RSC Advances

PAPER

View Article Online
View Journal | View Issue

Cite this: *RSC Adv.*, 2017, **7**, 40727

Synthesis of 3D porous MoS_2/g-C_3N_4 heterojunction as a high efficiency photocatalyst for boosting H_2 evolution activity†

Youzhi Cao,[a] Qin Gao,[c] Qiao Li,[a] Xinbo Jing,[a] Shufen Wang*[b] and Wei Wang*[a]

Received 18th June 2017
Accepted 11th August 2017

DOI: 10.1039/c7ra06774g

rsc.li/rsc-advances

A novel strategy was applied for the preparation of MoS_2/graphitic carbon nitride (g-C_3N_4) with porous morphology. These composites demonstrate a greatly enhanced response to visible light, and remarkably enhanced hydrogen evolution performance by photocatalytic water splitting. Compared to pure g-C_3N_4, the bulk doping porous MoS_2/g-C_3N_4 (BPMCN) heterojunction photocatalysts exhibit significantly enhanced H_2 evolution of 1640 μmol g^{-1} h^{-1} under visible light irradiation. The absorption edge is transfered from 455 nm (g-C_3N_4) to 532 nm (BPMCN-0.7) in the UV-vis diffuse reflectance spectra. Of course, structural, optical and electronic analyses demonstrate that the highly efficient activity of BPMCN is attributed to the enhanced light harvesting by efficient separation of photogenerated electron–hole pairs, and the expansion of the light response range. The present work shows that the formation of 3D heterojunction should be a good strategy to design efficient photocatalysts.

1. Introduction

Hydrogen is regarded as a very significant potential fuel. In particular, with photocatalysis technology development, photocatalytic hydrogen production through water splitting has been considered as a green, pure and high efficient technique and has attracted growing attention in the past few decades. Various kinds of photobased catalysts suitable for natural light have been developed.[1–4] Graphitic carbon nitride (g-C_3N_4), only composed of C and N elements, draws extensive attention due to its potential application in solar energy conversion, electrocatalysis, photo-synthesis, and bio-imaging, with an appropriate bandgap and excellent chemical stability. However, the efficiency of pure g-C_3N_4 is still far from being satisfactory owing to its small surface area and a high recombination rate of photoinduced electron–hole pairs.[5–7]

Up to now, to improve the efficiency of water-splitting, many strategies including doping with heteroatoms, deposition with metal atoms, coupling g-C_3N_4 with other semiconductors and two dimensional transition-metal dichalcogenides (TMDC) materials have been developed to improve the overall activity for photocatalytic processes.[8–14] One of the most studied members of the TMDC family is molybdenum disulfide (MoS_2), owing to its natural abundance, low cost, high chemical stability and good catalytic performance. Recently MoS_2 has become a representative non-precious material for photocatalytic hydrogen evolution reaction of water splitting.[15–17] Unfortunately, bulk MoS_2 has poor conductivity, which is attributed to the lateral transfer of electrons along the layered structure of MoS_2 nanosheets.[18,19] To date, its potential as a cocatalyst for photocatalytic H_2 production has received only sporadic attention even though it has demonstrated high activity in reactions involving H_2 under heterogeneous catalysis.[20]

Porous structures are more attractive due to their outstanding properties of low density and high surface area.[21,22] These can optimize the light-harvesting ability, mobility of charge carriers and permeability for mass transport. Therefore, the efficient light-induced redox reaction can be achieved.[23] Indeed, porous inorganic structured semiconductor materials (such as TiO_2, SnO_2, CdS, CdTe, Cu_2O, *etc.*) have exhibited promising applications in the field of photocatalytic water splitting for hydrogen production.[24–29]

Much work so far has focused on the synthesis of the surface doping MoS_2/g-C_3N_4 photocatalyst for water splitting.[8–10,30–34] However, further efforts are required to study the bulk doping MoS_2/g-C_3N_4 for photocatalytic H_2 evolution. Herein, we report a facile approach to synthesise porous MoS_2/g-C_3N_4 (BPMCN) heterojunction catalysis for enhancing photocatalytic hydrogen evolution. The synthetic process is illustrated in Fig. 1 with two steps: (1) preparation of mixed precursors using freeze drying; (2) annealing of mixed precursors at 600 °C to obtain porous MoS_2/g-C_3N_4 heterojunction photocatalysts. 3D porous MoS_2/g-C_3N_4 samples display enhanced photoabsorption, efficient

[a]School of Chemistry and Chemical Engineering, Key Laboratory for Green Processing of Chemical Engineering of Xinjiang Bingtuan, Shihezi University, Shihezi 832003, China. E-mail: wangwei_group@sina.com

[b]College of Sciences, Shihezi University, Shihezi 832003, China

[c]Key Laboratory of Synthetic and Natural Functional Molecule Chemistry of Ministry of Education, College of Chemistry and Material Science, Northwest University, Xi'an 710127, P. R. China

† Electronic supplementary information (ESI) available. See DOI: 10.1039/c7ra06774g

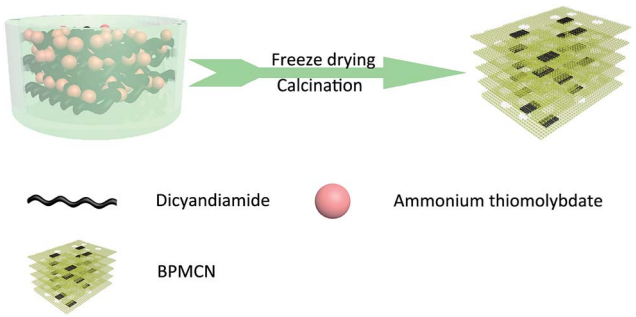

Fig. 1 Schematic illustration for the preparation of BPMCN photocatalyst.

charge separation and much higher photocatalytic activity compared to conventional g-C_3N_4 obtained by direct calcination of dicyandiamide.

2. Experimental

2.1. Chemicals

Dicyandiamide ($C_2H_4N_4$, CP), ammonium tetrathiomolybdate ($H_8MoN_2S_4$, AR), and other chemicals involved were purchased from Sinopharm Chemical Reagent Co., Ltd. (China) and used directly for experimental without further purification. All aqueous solutions throughout were prepared with the deionized water.

2.2. Sample preparation procedure

2.2.1 Preparation of bulk g-C_3N_4. Graphitic carbon nitride was synthesized using dicyandiamide (DCDA). In a typical run, the precursor was put in a lidded high quality alumina crucible, then placed inside a tube furnace and heated to 600 °C with a speed of 5 °C min^{-1} for 4 hours in Ar flow. The resultant powders were then washed with water to remove all unreacted and potentially detrimental surface species. The products were denoted as g-C_3N_4.

2.2.2 Preparation of bulk doping porous MoS_2/g-C_3N_4 (BPMCN). 1.5, 3, 6, 12 mg ammonium tetrathiomolybdate (AT) was mixed with 20 mg ml^{-1} (50 ml) DCDA in aqueous water respectively. And all were kept in liquid nitrogen, followed by freeze drying, the different porous-structured DCDA/AT precursors were obtained. Then calcinations of these porous-structured DCDA/AT from room temperature to 600 °C with a ramp rate of 2.3 °C min^{-1} in Ar flow and stabilized for 2 hours, the obtained samples were designated as BPMCN-0.25, BPMCN-0.7, BPMCN-1.8 and BPMCN-2.5 respectively.

2.3. Characterization

X-ray diffraction (XRD) was carried out on a BrukerAXS D8 X-ray diffractometer a Cu-Ka X-ray source operating at 40 kV and 40 mA. The morphologies of the samples were observed using a scanning electron microscope (SEM, JEOL JSM-6490LV) and a transmission electron microscope (TEM, FEI Tecnai G2). X-ray photoelectron spectroscopic (XPS) measurements were made on an Escalab 250Xi system. UV-vis diffuse reflection spectra (DRS) of the as-prepared products were carried out using an Evolution 220 UV-vis spectrophotometer (Thermo Fisher) from 200 to 800 nm. Fourier transform infrared (FT-IR) spectra of the samples were measured by a Nicolet 5700 Fourier transform infrared spectrometer. The photoluminescence spectra (PL) of the samples was obtained using a fluorescence spectrometer (Hitachi F-4500) at 293 K. The photocurrent response curves (PR) and electrochemical impedance spectroscopy (EIS) plots were collected by a CHI660 electrochemical analyzer.

2.4. Photocatalytic tests

The photocatalytic H_2 evolution reactions were performed in a gas-tight circulation system with a side window. 0.02 g photocatalyst powder was suspended in 90 ml aqueous solution containing 10 vol% triethanolamine as a sacrificial agent, loading 3 wt% Pt as cocatalyst by photodeposition of $H_2PtCl_6 \cdot 6H_2O$. The suspensions were stirred and irradiated under a 300 W Xe lamp with a cutoff filter ($\lambda > 400$ nm) (Fig. S1†). Prior to irradiation, suspensions were dispersed by sonication for 5 min and Ar was purged through the system for 25 min to remove oxygen. The amount of evolved H_2 was detected by an online gas chromatography (Agilent 7890, TCD) with Argon as the carrier gas.

2.5. Electrochemical measurements

Photoelectrochemical measurements were performed in a three-electrode, with single compartment quartz cell on an electrochemical station (CHI 660). Samples on ITO glass with an active area of *ca.* 1.0 cm^2 (1 mg of photocatalyst) were prepared as the working electrode. The platinum sheet and saturated calomel electrode (SCE) were served as the counter electrode and reference electrode, respectively. Besides, a bias voltage of 0.5 V was used for driving the photo-generated electrons transfer from the working electrode to the platinum electrode. The light source (300 W xenon lamp) with ultraviolet filter ($\lambda > 400$ nm) was mounted 10.0 cm away from the photoelectrochemical cell. A 0.50 M Na_2SO_4 aqueous solution worked as the electrolyte.

3. Results and discussion

The XRD patterns of the as-prepared pure g-C_3N_4, and BPMCN samples with different weight ration are shown in Fig. 2a. Two distinct diffraction peaks at 13.04° and 27.47° in the g-C_3N_4 and

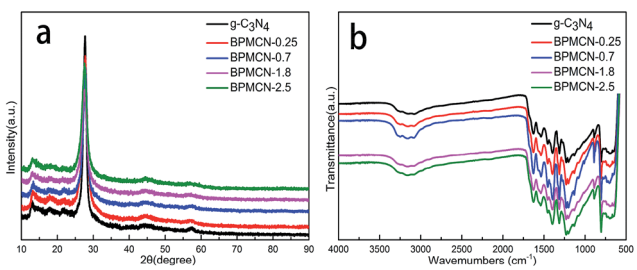

Fig. 2 (a) XRD patterns of BPMCN, (b) FT-IR spectra of BPMCN.

BPMCN samples, corresponding to the in-plane structural packing motif and interlayer stacking of aromatic segments, respectively, can be indexed as the (100) and (002) crystal planes for graphitic materials. This result reveals that the synthesized samples are graphitic carbon nitride. While no distinct MoS_2 diffraction peaks could be observed in the BPMCN samples. This might be attributed to the small amount of MoS_2 contents, having small amount of MoS_2 contents in the surface of g-C_3N_4 and highly dispersion in the interior of polymeric g-C_3N_4 photocatalysts. The presence of MoS_2 in the BPMCN samples could be confirmed by EDX elemental mapping and XPS analyses, as discussed later.[30] And the diffraction peaks at 14.0°, 33.4° and 58.7° are in good agreement with the (002), (100) and (110) planes of the hexagonal phase of MoS_2 in Fig. S2.†

The chemical structure of the pure g-C_3N_4 and BPMCN samples is confirmed by the FTIR spectra as shown in Fig. 2b. Several strong absorption bands in the range of 1200–1650 cm^{-1} are originated from the skeletal stretching of C–N heterocycles with peaks positioned at 1632, 1573, 1423, 1329 and 1245 cm^{-1}, comprising both trigonal N–$(C)_3$ (full condensation) and bridging C–NH–C units (partial condensation), which exemplifies the successful development of the extended C–N–C network. The broad peak between 3500 and 3000 cm^{-1} is originated from the N–H and O–H stretches, suggesting the free amino groups and adsorbed hydroxyl species on the surface of the nanosheets. Moreover, the characteristic breathing mode of the triazine units is observed at 802 cm^{-1}.

Further observation, the characteristic peaks of the BPMCN samples are found to be almost identical to the pure g-C_3N_4, inferring that the impregnation of MoS_2 don't destroy the in-plane tri-*s*-triazine units. The BPMCN samples reveal almost similar characteristic features to the pure g-C_3N_4, verifying that the structural integrity of g-C_3N_4 remain after the incorporation with MoS_2. The virtually identical X-ray diffraction patterns and FT-IR spectrum of g-C_3N_4 and the BPMCN samples reveal that loading with MoS_2 does not change the bulk structure of g-C_3N_4.[35] We further study the chemical composition and chemical states of BPMCN-0.7 by X-ray photoelectron spectroscopy (XPS) and shown in Fig. 3. The C 1s spectra of the sample shows two peaks, which are located at 284.6 eV and 288.0 eV. The peak at 284.6 eV is typically ascribed to graphite sp^2 C–C bonds in adventitious carbon species. The peak at 288.0 eV is ascribed to the sp^2 hybridized carbon bonded to N in the C–N–C coordination. The N 1s peak for the BPMCN-0.7 can be deconvoluted into three peaks with binding energy at 398.9, 399.8, and 401.0 eV (Fig. 3c). The peak at 398.9 eV is assigned to sp^2-hybridized N(C=N–C), and the other two peaks at 399.8 and 401.0 eV are ascribed to tertiary N (N–$(C)_3$) and amino functional groups with a H atom (C–N–H), respectively. A weak O 1s peak at 532.1 eV is attributed to the adsorbed H_2O or CO_2, which is a common phenomenon found in literatures (Fig. 3d).[3] To verify the state of S in the BPMCN-0.7, we further analyze the high-resolution S 2p spectra, which shows two peaks at 162.44 (S^{2-}) and 169.11 (S^{4-}) eV, corresponding to the S 2p3/2 A and S 2p1/2 B respectively.[36] For Mo 3d spectra, two peaks, accredited to the doublet Mo 3d5/2 and Mo 3d3/2, are located at 229.38 and 232.35 eV (Fig. 3f). Those results indicate the existence of Mo^{4+} and S^{2-}, with an atomic composition ratio for Mo and S of

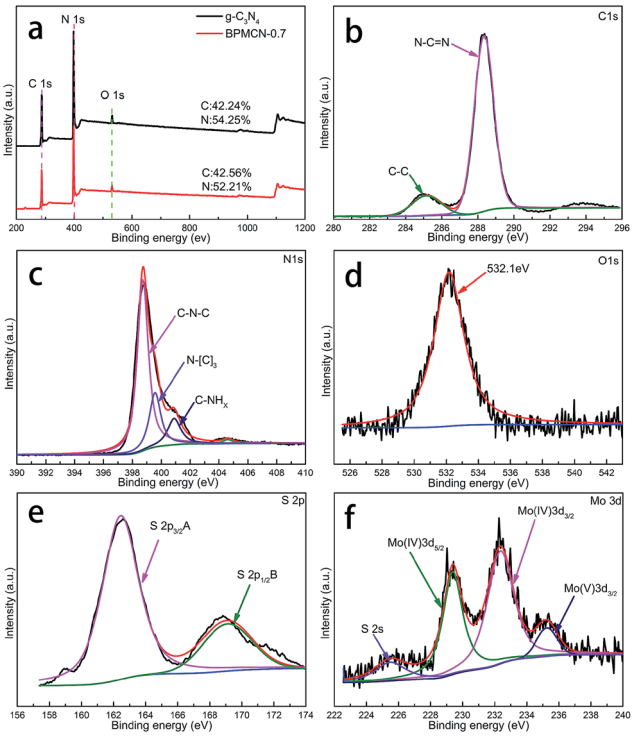

Fig. 3 XPS spectra of as-fabricated photocatalysts: (a) survey of g-C_3N_4 and BPMCN-0.7 and (b) C 1s; (c) N 1s; (d) O 1s; (e) S 2p; (f) Mo 3d of BPMCN-0.7.

1 : 2. Of course, the C/N atomic ratio of the BPMCN-0.7 is same as pure g-C_3N_4, which is 0.77 and also indicates the structure of g-C_3N_4 is not destroyed with loading MoS_2.

In order to verify the detail morphology of the BPMCN heterojunction photocatalysts, TEM has been introduced. As shown in Fig. 4a, compared with pure g-C_3N_4 (Fig. 4c), the as prepared BPMCN samples with porous morphology exhibit black lamellar feature with transparent parts, indicating it possesses the porous structure. The porous morphology of the BPMCN-0.7 was also investigated *via* scanning electron microscopy (SEM). As shown in Fig. 4b, the BPMCN-0.7 still maintain porous and irregular 3D morphology, although a great portion of g-C_3N_4 sheets is stacked. Its morphology is quite different from that of the pure g-C_3N_4 with a typical layer structure stacked layer by layer (Fig. 4d). To determine the presence of MoS_2, EDX elemental mappings are carried out and the results are shown in Fig. 5. Elemental mappings reveal that the BPMCN-0.7 mainly contains five elements (C, N, O, S and Mo), which is coincident with the results of XPS (Fig. 3).

Fig S3 and S4† display the nitrogen adsorption–desorption isotherms and Barrett–Joyner–Halenda (BJH) pore-size distribution curves of the g-C_3N_4 and BPMCN samples. It is obvious that the nitrogen adsorption–desorption isotherms (Fig. S3†) for pure g-C_3N_4 and MoS_2/g-C_3N_4 heterojunction catalysts belong to type IV, which suggests the presence of mesopores. The surface areas and pore volumes (Table S1†) of BPMCN-0.7 (31.92 m^2 g^{-1} and 0.19 cm^3 g^{-1}) are significantly higher than those of other BPMCN samples and g-C_3N_4 (4.48 m^2 g^{-1} and

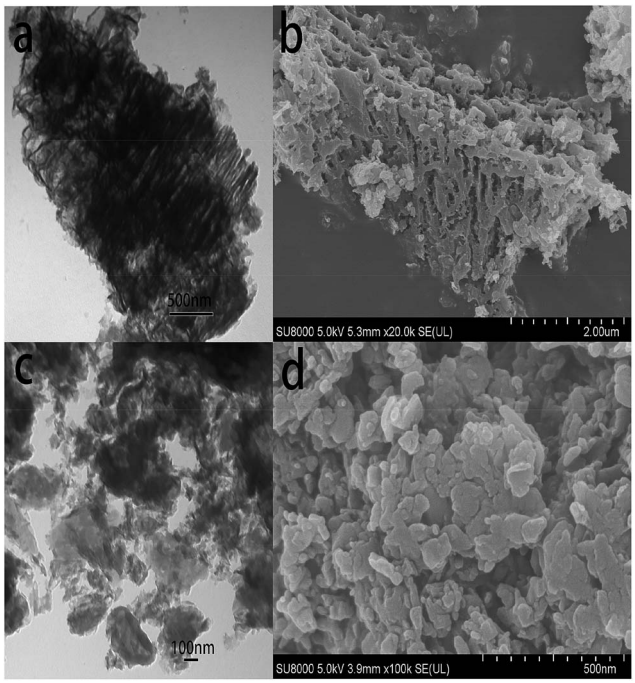

Fig. 4 (a) Typical TEM images and (b) SEM images of BPMCN-0.7, (c) TEM images and (d) SEM images of g-C_3N_4.

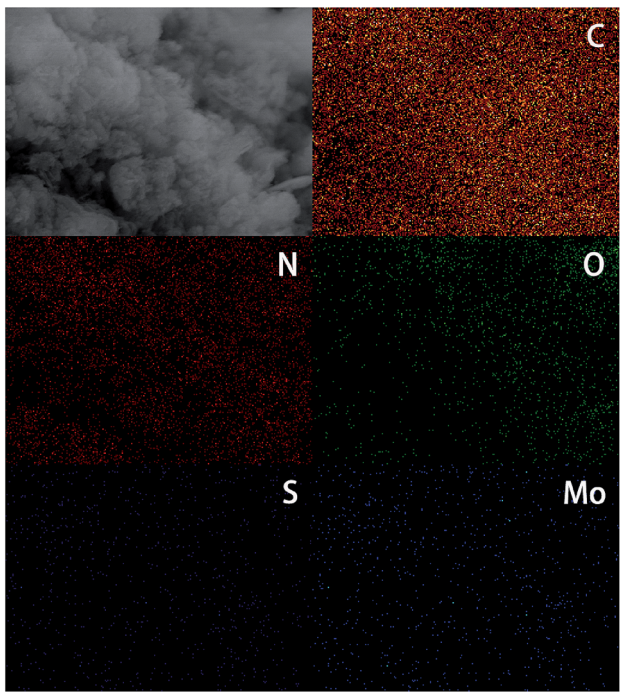

Fig. 5 Elemental mapping pattern of BPMCN-0.7.

0.025 $cm^3 g^{-1}$). The pore size distribution of the samples further confirms the formation of mesopores. Mesopores and macropores can be observed in the all sample. The mesopores can be ascribed to the pores formed between the layers, whereas the macropores are the pores on the surface of the layers, as observed in the TEM and SEM image (Fig. 4). The BPMCN-0.7 displays the biggest surface area and pore volume, which is consistent with the results of photocatalytic activity. Therefore, the higher surface area would contribute to the higher photocatalytic activity of the BPMCN-0.7.

To test whether the introduction of MoS_2 could improve the photocatalytic efficiency of g-C_3N_4 in the presence of TEOA, we investigated the g-C_3N_4 and BPMCN samples as heterogeneous photocatalysts for water splitting to produce hydrogen under visible light (>400 nm). Meanwhile, we studied the influence of the MoS_2 amount in the BPMCN samples on the photocatalytic activity under the same conditions. As shown in Fig. 6a and c, the photocatalytic H_2 evolution rate of pure g-C_3N_4 is only 267 μmol g^{-1} h^{-1}. After the impregnation of MoS_2, all the BPMCN photocatalysts show enhanced H_2 evolution activity than pure g-C_3N_4. With the content of MoS_2 increase, the amount of H_2 first increases and then decreases. The sample with optimal photocatalytic H_2 evolution rate is BPMCN-0.7 with H_2 evolution of 1640 μmol g^{-1} h^{-1}, exhibiting about 6-fold increment compared to pure g-C_3N_4, which is consistent with the result of BET. Without the addition of TEOA, no H_2 was detected in the visible light irradiation, mainly due to the high recombination rate of electron–hole pair and the low sensitivity of the detector, which shows that TEOA can separate electron–hole pairs and boost the efficiency of hydrogen production through water splitting. Recently, a report is related to the explored MoS_2/g-C_3N_4 heterostructure for H_2 production, its hightest H_2 evolution rate reaches 23.1 μmol h^{-1} (100 mg photocatalyst, $\lambda > 400$ nm).[37] However, our work indicates H_2 production rate of 32.8 μmol h^{-1} only need 20 mg photocatalyst, which exhibits that our work possesses a potential in the field of photocatalytic water splitting for H_2 production. Furthermore, the stability of BPMCN-0.7 was tested by using the same condition for photocatalytic H_2 production repeatedly five times under visible-light irradiation (Fig. 6b and d). No obvious deactivation of the catalytic activity is observed for BPMCN-0.7 upon

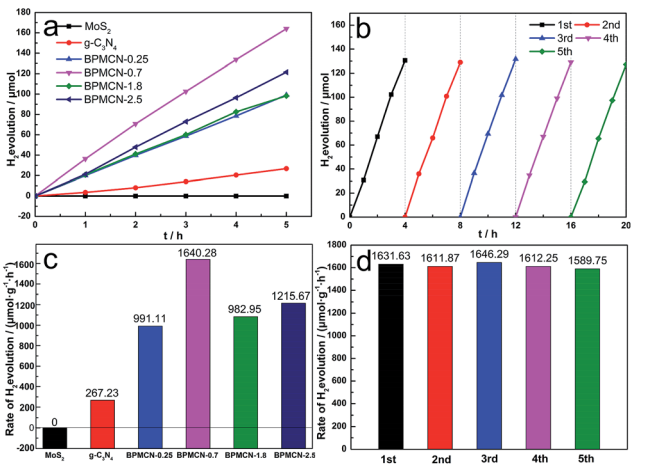

Fig. 6 Photocatalytic activity of the photocatalysts (0.020 g) under visible light (a) and (c) H_2 evolution rates of the MoS_2, g-C_3N_4 and BPMCN samples in an aqueous solution (90 ml) containing TEOA (10 mL) as the sacrificial agent; (b) and (d) recycling test of BPMCN-0.7 (0.020 g).

circulation duration, indicating the high stability of the BPMCN photocatalysts during photocatalytic H_2 production.

Of course, two methods can be applied to the fields of improving the photocatalytic activity. The first one is to extend the absorption edge. The second is to improve the separation efficiency of photogenerated charge. To confirm the reasons for enhanced activity of the samples, we conducted UV-vis diffuse reflectance spectra and the band gap values calculated by plots of $(F(R)E)^{1/2}$ *versus* photo energy. As shown in Fig. 7a, the characteristic absorption edge of g-C_3N_4 is at approximately 455 nm, originating from its intrinsic band gap of 2.72 eV, which has limited visible light absorption ability for itself.[13] After introduction of MoS_2, the band gap of BPMCN-0.7 is only about 2.33 eV, corresponding to the absorption edge of 532 nm. The absorption edge is transferred from 455 nm to 532 nm.

Photoluminescence (PL), caused by the recombination of charge carriers, could also provide a measurement method for the efficiency of the charge carrier trapping, transfer and separation in the samples. As shown in Fig. 7b, the PL intensity for BPMCN-0.7 decreases significantly compared to g-C_3N_4. In general, a decrease in the PL intensity indicates a suppressed electron–hole pair recombination, which makes BPMCN-0.7 generate more photoelectrons and holes to participate in the photocatalytic reaction. This may be because the heterojunction formed at the interior and interface between g-C_3N_4 and MoS_2 with a high rate of carrier mobility can restrain the recombination of photogenerated charge effectively and accelerate charge transport.

The photogenerated charge separation and electron transfer performance of the BPMCN system were also studied using electrochemical impedance spectroscopy (EIS) and photocurrent responses. The Nyquist plots of g-C_3N_4 and BPMCN-0.7 are performed to investigate the effect of MoS_2 doping. Generally, a smaller arc size reflects smaller charge transfer resistance on the electrode surface. As shown in Fig. 7c, the arc radius on the EIS plots of BPMCN-0.7 is smaller than that of g-C_3N_4 under visible light, suggesting that the separation and transfer efficiency of photogenerated electron and hole pairs is greatly increased through an interfacial interaction between g-C_3N_4 and MoS_2.

Fig. 7d shows the photocurrent responses *via* four on–off cycles for bulk the g-C_3N_4, MoS_2 and BPMCN-0.7 materials cast on indium tin oxide glasses. The photocurrents of the BPMCN-0.7 sample were fast and uniform with high reproducibility under visible light irradiation, indicating stable electrodes and a relative reversible photoresponse. It is clear that the BPMCN-0.7 has a higher photocurrent density than that of bulk g-C_3N_4, which can be ascribed to the existence of heterojunction between MoS_2 and g-C_3N_4, where photogenerated electrons and holes could be efficiently separated in space and the photogenerated carrier recombination will be reduced. As a result, the BPMCN-0.7 sample show enhanced photocurrent. The improved transfer efficiency of charge carriers could lead to the enhanced photocatalytic activity of BPMCN photocatalysts.

Since photoluminescence spectra, electrochemical impedance spectroscopy and photocurrent response are regarded as valid evidences of photogenerated charge separation, these phenomena indicate the improvement of the separation efficiency of photogenerated charge. We consider that the morphology characteristics of material with the porous structure and MoS_2/g-C_3N_4 heterojunction cause the enhanced photocatalytic H_2 evolution. For the BPMCN, its porous structure with a greater specific surface area and pore volume is richer than the pure g-C_3N_4, which may lead to multiple reflections of incident light within the porous channel of the BPMCN and more MoS_2/g-C_3N_4 heterojunction exposed on the surface of the porous channel. It improves the utilization rate of visible light and further expands the visible absorption edge. Meanwhile, the existence of heterojunction between MoS_2 with g-C_3N_4 in the interior and surface can more effectively prevent recombination of photogenerated electrons and holes.

According to UV-vis diffuse reflection spectra and VBXPS (Fig. 7a and S5†), the bottom conduction band and top valence band potentials of g-C_3N_4 and BPMCN-0.7 are calculated to be −0.62, +2.1, −0.52 and +1.8 V in Fig. 8. In addition, the valence and condition band of MoS_2 are consistent with the reported work owing to the similar synthesis strategy.[33] The MoS_2, as a semiconductor, can form heterojunction with g-C_3N_4.[34,37] I-type heterojunction, which is that the bottom conduction band and top valence band potentials of the MoS_2 locate in the forbidden band of the g-C_3N_4, is observed in MoS_2/g-C_3N_4 samples. The photocatalytic hydrogen evolution mechanism of BPMCN under visible light illumination is showed in Fig. 8. At first, the electrons in the valence band (VB) of g-C_3N_4 were excited to its conduction band (CB) under irradiation, forming the electron–hole pairs. Then, the photoexcited electrons would transfer from g-C_3N_4 to MoS_2 and Pt and the separated electrons on the surface of MoS_2 and Pt would combine with absorbed H^+ to produce H_2. TEOA, as a sacrificial agent of h^+, was introduced into the reaction system. With the decrease of h^+, the balance moves to the direction which can produce holes and electrons. The mentioned factor would produce a large amount of electrons and improve the separation efficiency of photogenerated

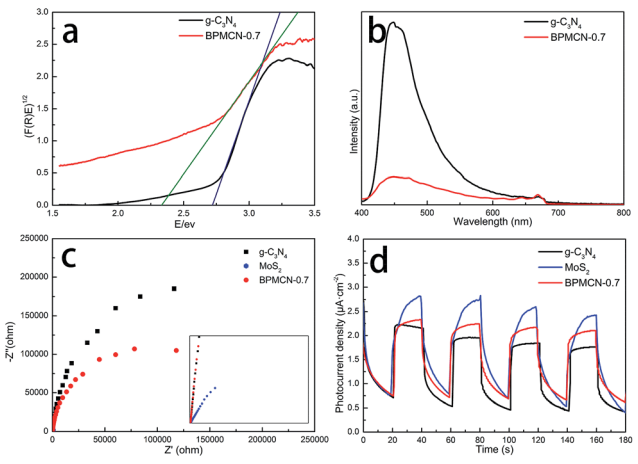

Fig. 7 (a) The plot of $(F(R)E)^{1/2}$ *versus* energy (E) for the band gap energy of g-C_3N_4 and BPMCN-0.7 samples; (b) PL spectra, (c) electrochemical impedance spectroscopy and (d) transient photocurrent response for the MoS_2, g-C_3N_4 and BPMCN-0.7 samples.

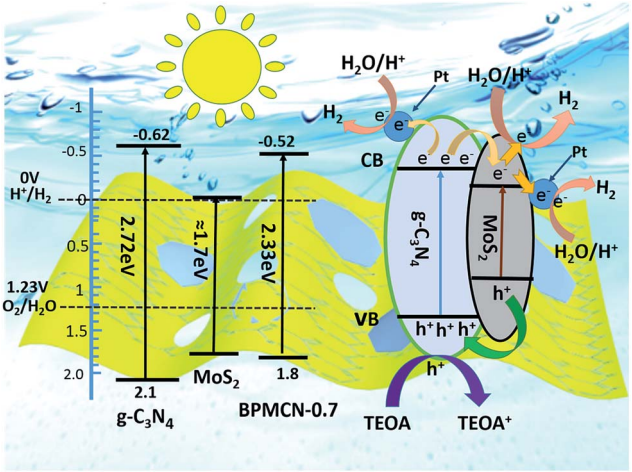

Fig. 8 Photocatalytic H_2 production mechanism for BPMCN.

electron–hole pairs, resulting in the improvement of photocatalytic H_2 production efficiency.

4. Conclusions

In summary, a new kind of composite photocatalyst of porous MoS_2/g-C_3N_4 heterojunction has been successfully prepared *via* a novel method called bulk doping strategy. The photocatalytic hydrogen evolution experiments indicate that the MoS_2 can efficiently promote the separation of photogenerated charge carriers in g-C_3N_4, extend light response range, and greatly enhance photocatalytic performance in hydrogen production by water splitting under visible light irradiation. The optimum photocatalytic H_2 evolution rate on BPMCN-0.7 reaches 1640 μmol g^{-1} h^{-1}, which is enhanced by 6 times compared to the bulk g-C_3N_4. Besides, the BPMCN-0.7 also shows excellent recyclability and chemical stability. This work demonstrates that MoS_2 can be a promising semiconductor for developing high efficiency photocatalyst with potential applications in hydrogen production and solar energy utilization.

Conflicts of interest

There are no conflicts to declare.

Acknowledgements

The work was supported by the National Natural Science Foundation of China (grant No. 21267020).

Notes and references

1 G. Zhang, G. Li and X. Wang, *ChemCatChem*, 2015, **7**, 2864–2870.
2 Q. Liang, Z. Li, Z.-H. Huang, F. Kang and Q.-H. Yang, *Adv. Funct. Mater.*, 2015, **25**, 6885–6892.
3 D. J. Martin, K. Qiu, S. A. Shevlin, A. D. Handoko, X. Chen, Z. Guo and J. Tang, *Angew. Chem., Int. Ed.*, 2014, **53**, 9240–9245.
4 Y. S. Jun, J. Park, S. U. Lee, A. Thomas, W. H. Hong and G. D. Stucky, *Angew. Chem.*, 2013, **52**, 11083–11087.
5 S. Cao and J. Yu, *J. Phys. Chem. Lett.*, 2014, **5**, 2101–2107.
6 Z. Zhao, Y. Sun and F. Dong, *Nanoscale*, 2015, **7**, 15–37.
7 F. Fresno, R. Portela, S. Suárez and J. M. Coronado, *J. Mater. Chem. A*, 2014, **2**, 2863–2884.
8 Q. Li, N. Zhang, Y. Yang, G. Wang and D. H. L. Ng, *Langmuir*, 2014, **30**, 8965–8972.
9 D. Zheng, G. Zhang, Y. Hou and X. Wang, *Appl. Catal., A*, 2016, **521**, 2–8.
10 X. Lu, Y. Jin, X. Zhang, G. Xu, D. Wang, J. Lv, Z. Zheng and Y. Wu, *Dalton Trans.*, 2016, **45**, 15406–15414.
11 W. Li, C. Feng, S. Dai, J. Yue, F. Hua and H. Hou, *Appl. Catal., B*, 2015, **168–169**, 465–471.
12 D. Chen, Z. Wang, D. Yue, G. Yang, T. Ren and H. Ding, *J. Nanosci. Nanotechnol.*, 2016, **16**, 471–479.
13 J. Qin, J. Huo, P. Zhang, J. Zeng, T. Wang and H. Zeng, *Nanoscale*, 2016, **8**, 2249–2259.
14 Z. Chen, S. Pronkin, T. P. Fellinger, K. Kailasam, G. Vile, D. Albani, F. Krumeich, R. Leary, J. Barnard, J. M. Thomas, J. Perez-Ramirez, M. Antonietti and D. Dontsova, *ACS Nano*, 2016, **10**, 3166–3175.
15 J. Deng, H. Li, S. Wang, D. Ding, M. Chen, C. Liu, Z. Tian, K. S. Novoselov, C. Ma, D. Deng and X. Bao, *Nat. Commun.*, 2017, **8**, 14430.
16 S. Zhang, B. V. R. Chowdari, Z. Wen, J. Jin and J. Yang, *ACS Nano*, 2015, **9**, 12464–12472.
17 X. Cao, C. Tan, X. Zhang, W. Zhao and H. Zhang, *Adv. Mater.*, 2016, **28**, 6167–6196.
18 X. Zhang, Z. Lai, C. Tan and H. Zhang, *Angew. Chem.*, 2016, **55**, 8816–8838.
19 S. S. Chou, B. Kaehr, J. Kim, B. M. Foley, M. De, P. E. Hopkins, J. Huang, C. J. Brinker and V. P. Dravid, *Angew. Chem., Int. Ed.*, 2013, **52**, 4160–4164.
20 X. Zhang, Z. Lai, C. Tan and H. Zhang, *Angew. Chem., Int. Ed.*, 2016, **55**, 8816–8838.
21 Z.-F. Huang, J. Song, L. Pan, Z. Wang, X. Zhang, J.-J. Zou, W. Mi, X. Zhang and L. Wang, *Nano Energy*, 2015, **12**, 646–656.
22 Z. Wang, W. Guan, Y. Sun, F. Dong, Y. Zhou and W.-K. Ho, *Nanoscale*, 2015, **7**, 2471–2479.
23 H. Tong, S. Ouyang, Y. Bi, N. Umezawa, M. Oshikiri and J. Ye, *Adv. Mater.*, 2012, **24**, 229–251.
24 F.-Y. Su and W.-D. Zhang, *Chem.–Asian J.*, 2017, **12**, 515–523.
25 L. Shi, K. Chang, H. Zhang, X. Hai, L. Yang, T. Wang and J. Ye, *Small*, 2016, **12**, 4431–4439.
26 X. Chen, H. Li, Y. Wu, H. Wu, L. Wu, P. Tan, J. Pan and X. Xiong, *J. Colloid Interface Sci.*, 2016, **476**, 132–143.
27 S. P. Adhikari, G. P. Awasthi, H. J. Kim, C. H. Park and C. S. Kim, *Langmuir*, 2016, **32**, 6163–6175.
28 X. Pan, X. Chen and Z. Yi, *ACS Appl. Mater. Interfaces*, 2016, **8**, 10104–10108.
29 H.-J. Li, B.-W. Sun, L. Sui, D.-J. Qian and M. Chen, *Phys. Chem. Chem. Phys.*, 2015, **17**, 3309–3315.

30 Y. Cao, Q. Li and W. Wang, *RSC Adv.*, 2017, **7**, 6131–6139.
31 H. Yu, P. Xiao, P. Wang and J. Yu, *Appl. Catal., B*, 2016, **193**, 217–225.
32 J. Yan, Z. Chen, H. Ji, Z. Liu, X. Wang, Y. Xu, X. She, L. Huang, L. Xu, H. Xu and H. Li, *Chemistry*, 2016, **22**, 4764–4773.
33 Y. Hou, A. B. Laursen, J. Zhang, G. Zhang, Y. Zhu, X. Wang, S. Dahl and I. Chorkendorff, *Angew. Chem.*, 2013, **52**, 3621–3625.
34 S. A. Ansari and M. H. Cho, *Sci. Rep.*, 2017, **7**, 43055, DOI: 10.1038/srep43055.
35 W.-J. Ong, L.-L. Tan, S.-P. Chai, S.-T. Yong and A. R. Mohamed, *Nano Energy*, 2015, **13**, 757–770.
36 X. Ding, W. Ho, J. Shang and L. Zhang, *Appl. Catal., B*, 2016, **182**, 316–325.
37 Y. Tian, L. Ge, K. Wang and Y. Chai, *Mater. Charact.*, 2014, **87**, 70–73.